A Novel SiC-Based Multifunctional Onboard Battery Charger for Plug-In Electric Vehicles

Hoang Vu Nguyen, *Member, IEEE*, Dong-Choon Lee, *Senior Member, IEEE*, and Frede Blaabjerg, *Fellow, IEEE*

***Abstract*—This article proposes a simple and effective method to reduce the bulky capacitor in onboard battery charger (OBC) where low-voltage (LV) battery charging circuit is utilized as an active power decoupling (APD) circuit to filter out the second-order ripple power. When the OBC is connected to the grid to charge the high-voltage (HV) battery, the switches on the primary side of the LV charging circuit are operated as those of an ac–dc converter with APD function. Consequently, small dc-link capacitors can be used instead of large capacitor banks. In the proposed OBC, the switching devices are shared for the ac–dc converter, APD circuit, and primary-side of the LV charger. For a simultaneous charging of the LV and HV batteries, a dc–dc converter is added, which shares the same transformer core and secondary side with the LV charging circuit. So the functions of the OBC are maintained in the proposed topology whereas the volume and cost are decreased by 52.3% and 46.9% compared with the conventional nonisolated OBC, respectively. A 2-kW SiC-based prototype has been designed and tested to verify the validity of the proposed system. The peak efficiencies of the OBC and LV charger are 96.1% and 95.3%, respectively.**

***Index Terms*—Low-voltage (LV) dc–dc converter, plug-in hybrid electric vehicles, single-phase onboard battery chargers (OBC).**

I. Introduction

NOWADAYS, electrification is the most promising solution to enable a more sustainable transportation system. Plug-in electric vehicles (PEVs) have become more popular in the global market. The battery charger is considered as one of the essential parts in PEVs and mainly determines the charging time of the vehicle. Thus, high efficiency and high-power density of the onboard battery charger (OBC) is the key design consideration [1].

By using wide band-gap power switches, a higher switching-frequency operation is possible with lower power losses [2]. Therefore, the power density of an OBC can be enhanced by reducing the size of passive components. However, in single-phase battery chargers, there is an inherent power ripple component that fluctuates with the double grid frequency, which causes dc-link voltage ripple. Conventionally, bulky dc-link capacitor banks are used to smoothen this low-frequency power ripple, which is a crucial barrier for obtaining high power density of the OBC.

In order to charge an HV battery by an OBC, the single-phase ac grid is used to supply the power. In this charging circuit, second-order harmonic current in the dc link is a serious issue in the ac–dc stage of the single-phase OBC [3]. In this case, the aluminum electrolytic capacitors or large film capacitor banks are required to filter out this power ripple. However, the lifetime of the electrolytic capacitors is a problem due to the thermal conditions of the vehicles [4]. Therefore, large film capacitor banks need to be adopted, which results in a considerable increase in the size and cost of chargers. Several active methods were proposed to avoid using large capacitor banks in a single-phase dc link [5]–[9]. A common approach is to use an additional active power filter, which is connected in parallel with the dc link to absorb the second-order ripple power. In these methods, an auxiliary circuit with active components is required, which increases the power loss, cost, and complexity of the whole system.

In the meanwhile, integrated power units have been proposed to enhance the power density of an OBC [10]–[17], which can reduce the weight, space, and cost of the charger. For this purpose, multifunctional converters have been proposed, which integrate HV and low-voltage (LV) charging circuits so that they can charge the HV battery for parking mode or the LV battery for driving mode. Some power switches in the ac–dc stage are shared for the HV and LV chargers to reduce the count of the components [10]. However, the efficiency of the LV circuit is low due to a high step-down ratio. Also, the ac–dc stage has to operate with high currents for LV charger and high voltage for HV charger. In [11] and [12], the integrated auxiliary power module composed of an active power filter and an LV battery charger was proposed, which can reduce the dc-link capacitance effectively, leading to the reduction of the overall size of the converter. However, these systems can only operate with unidirectional power flow. A similar concept was presented where the OBC can operate in three different modes: grid-to-vehicle (G2V), vehicle-to-grid (V2G), and HV-battery-to-LV-battery (H2L) modes [13], [14]. These topologies can achieve higher power density and lower cost, but the LV battery cannot be charged when the HV battery is charged. In addition, an integrated battery charger was proposed with the capability of simultaneous charging of the HV and

Manuscript received February 19, 2020; revised May 26, 2020 and August 4, 2020; accepted September 16, 2020. Date of publication September 23, 2020; date of current version January 22, 2021. This work was supported by the National Research Foundation of Korea grant funded by the Korea Government under Grant NRF-2017R1A2A2A05069629. Recommended for publication by Associate Editor A. K. Gupta. *(Corresponding author: Dong-Choon Lee.)*

Hoang Vu Nguyen and Dong-Choon Lee are with the Department of Electrical Engineering, Yeungnam University, Gyeongbuk 38541, South Korea (e-mail: nhvu20@gmail.com; dclee@yu.ac.kr).

Frede Blaabjerg is with the Department of Energy Technology, Aalborg University, 9220 Aalborg, Denmark (e-mail: fbl@et.aau.dk).

Color versions of one or more of the figures in this article are available online at https://ieeexplore.ieee.org.

Digital Object Identifier 10.1109/TPEL.2020.3026034

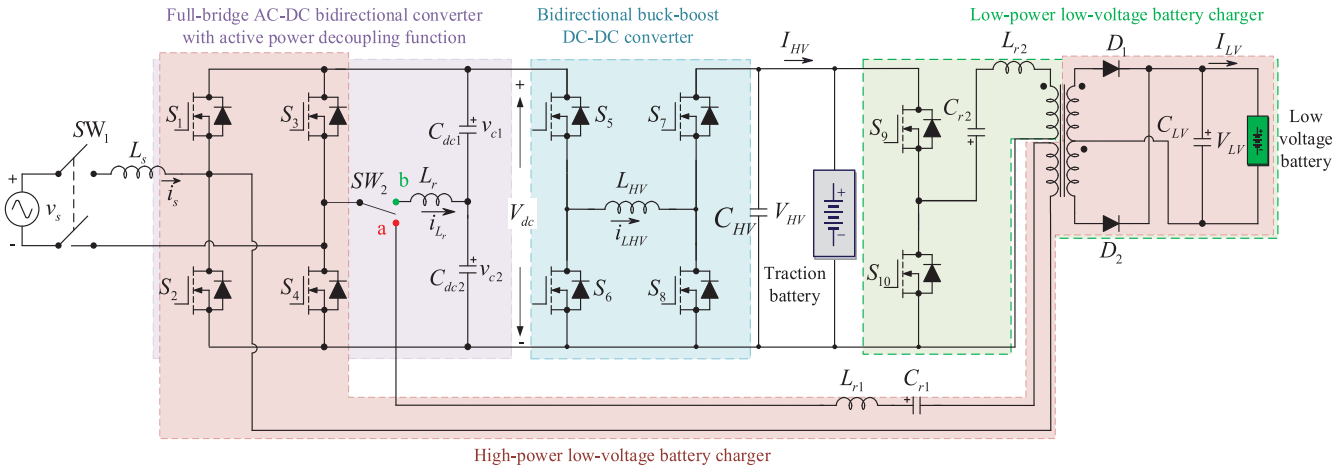

Fig. 1. Circuit configuration of the proposed multifunctional onboard battery charger.

LV batteries [15]. However, a large capacitor bank is needed, and the OBC cannot operate with bidirectional power flow. In [16] and [17], the three-port concept was presented, in which a single high-frequency transformer is used to provide the galvanic isolation for OBC and LV charging circuit. Furthermore, with this structure, it is possible to charge both the HV and LV batteries simultaneously. However, the integrated switches need to carry the total current for both HV chargers and LV chargers at the same time, which leads to an increase in the current rating of the switching devices. Besides, phase-shift modulation and duty cycle control are required, which can be challenging for battery chargers with a wide range of output voltage and power.

In this article, a novel nonisolated multifunctional OBC is proposed, where some components of the OBC and LV charger are shared. The active power decoupling (APD) function is provided without adding additional switching devices, which leads to a significant reduction of the dc-link capacitance. The switching devices of the ac–dc converter are used as the primary side of the isolated dc–dc converter for LV charging. Also, a half-bridge circuit is added to charge the LV battery during HV charging, which shares the transformer core and the secondary side with the LV charger. In this way, both the HV and LV batteries can be charged simultaneously. Furthermore, Both LV charging circuits are designed based on a series resonant converter to improve the efficiency of the LV charging circuit. Since small film capacitors are used in the dc link and the components of the OBC and LV charger are utilized in common, the cost, weight, and size of the proposed OBC can be reduced in comparison to those of the conventional nonisolated OBC. A 2-kW SiC-based prototype is built and tested to verify the effectiveness of the proposed OBC. The peak efficiencies of the HV and LV chargers are 96.1% and 95.3%, respectively.

The rest of the article is organized as follows. Section II presents the proposed multifunctional OBC and the operating modes. Section III discusses a design procedure and control strategy of the proposed OBC. In Section IV, the comparative analysis of the cost and volume is presented. Besides, some features of the proposed circuit are investigated with other converter topologies. Next, experimental results are shown in Section V. Finally, the conclusion is given in Section VI.

II. Proposed Multifunctional Onboard Battery Charger and Operating Principle

A. Configuration of the Proposed Onboard Battery Charger

The circuit configuration of the proposed multifunctional charger is shown in Fig. 1. The proposed OBC is composed of an H-bridge converter $(S_1 - S_4)$, three half-bridge circuits $(S_5 - S_6, S_7 - S_8, \text{and} S_9 - S_{10})$, two rectifier diodes $(D_1 - D_2)$, and a high-frequency transformer. The ac–dc converter plays a role in not only connecting the OBC to the ac grid but also charging the LV battery. In this proposed OBC, the front-end converter can work as an ac–dc converter, dc–ac inverter, and APD circuit. It can also be used as primary-side switches of the LV charger.

A nonisolated bidirectional buck–boost dc–dc converter is used to control the power flow between the dc link and HV battery. The nonisolated OBC can satisfy SAE J1772, which is the standard of the conductive charger for electric vehicles (EVs) since the traction battery ground is always floating with the chassis of the vehicle [18]. The traction battery has a wide range of operating voltage, so the dc–dc converter has to be able to function in both buck and boost operating modes. The dc–dc converter also works for the OBC or LV charging depending on the operating mode. The LV battery is charged from the HV battery through the buck–boost dc–dc converter and isolated high-power LV charging circuit (HP-LVC).

A low-power LV charging circuit (LP-LVC) is added to charge the LV and HV batteries simultaneously, which shares an isolated transformer core and secondary side with the LV charger. LLC resonant networks are adopted in both LV charging circuits to improve efficiency. The LV battery is mainly charged through the HP-LVC. The LP-LVC is operated, if necessary, only when the HV battery is being charged.

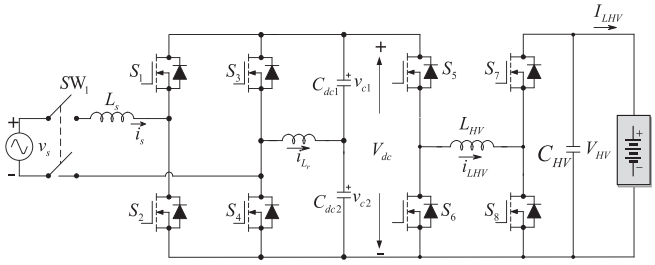

Fig. 2. Circuit operating in mode I (G2V) or mode II (V2G).

B. Operating Principle of the Proposed Charger

The proposed OBC has four different modes: G2V, V2G, H2L, and grid-to-LV-battery (GH2L) modes, where detailed descriptions for each mode are given as follows:

Mode I (G2V): In this mode, the HV battery is charged from the grid via ac–dc and dc–dc converters. The relay, SW_2, is connected to terminal *b* so that the proposed multifunctional circuit can operate as an APD circuit. The second-order ripple power can be absorbed by regulating the voltage waveform of the capacitors $C_{\rm dc1}$ and $C_{\rm dc2}$. Therefore, small film capacitors can be used instead of large capacitor banks. The ac–dc converter can be used to achieve sinusoidal input current at a power factor of unity. The bidirectional buck–boost dc–dc converter is used to control the current and voltage of the HV battery. The soft-switching technique is also applied to reduce the power losses of the dc–dc converter. Fig. 2 shows the circuit involved in mode I.

Mode II (V2G): In this mode, the HV battery provides energy back to the ac grid. SW_2 is still connected to terminal *b* to operate with APD function. The dc–dc converter is used to control the discharging current, whereas the ac–dc stage works as an inverter to control the grid current and dc-link voltage. This is also shown in Fig. 2.

Mode III (H2L): In this mode, SW_2 is connected to terminal *a*. The LV battery is charged via the buck–boost dc–dc converter and HP-LVC. During this period, the H-bridge converter $(S_1 - S_4)$of the ac–dc converter is used as the primary side of the LV charging circuit to form a full-bridge resonant LLC converter, which is shown in Fig. 3.

Mode IV (GH2L): The HV and LV batteries are charged at the same time using the OBC and LP-LVC. The circuit involved in this mode is shown in Fig. 4. The transformer core and the secondary side of the LP-LVC are shared with the HP-LVC. When the LV battery is fully charged, the operation of the circuit is changed to G2V mode.

III. Design of Proposed Multifunctional Onboard Battery Charger

In this section, a design procedure of the proposed OBC is described in detail, of which specification is listed in Table I. In this work, SiC MOSFETs are used, which have features of high switching frequency, low power loss, and high operating temperature. These points are preferably required for automobile applications. In addition, by operating SiC MOSFET devices with a soft-switching scheme, the overall efficiency of the topology can be further improved.

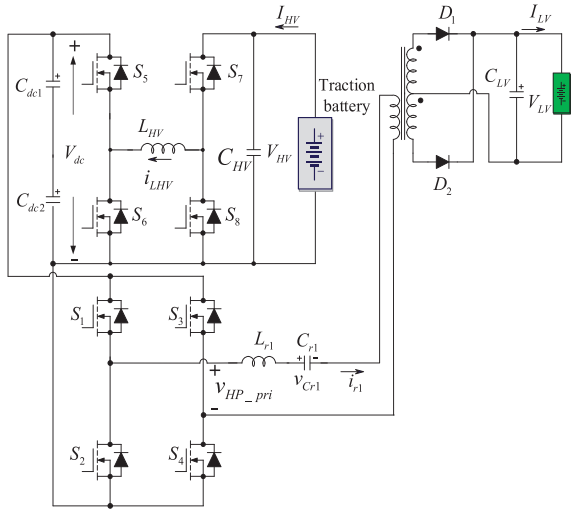

Fig. 3. High-power low-voltage charging circuit for mode III.

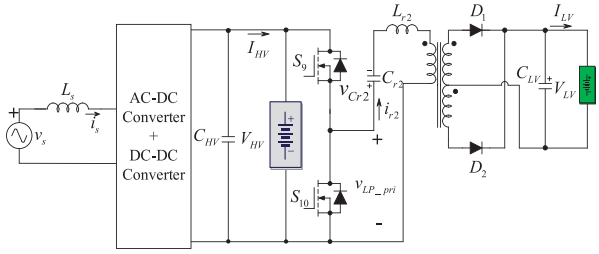

Fig. 4. Low-power low-voltage charging circuit for mode IV.

TABLE I
Design Specifications of the Proposed Onboard Battery Charger

Description	Values
Grid voltage	110 V rms
Grid frequency	60 Hz
Switching frequency	100 kHz
DC-link voltage	350 V
HV battery voltage	250- 430 V
HV charging power	2 kW
LV battery voltage	12 – 13 V
HP-LVC power	1 kW
LP-LVC power	0.5 kW

A. AC–DC Converter With APD Capability

The ac–dc converter of the proposed OBC uses small film capacitors in the dc link. To achieve the APD function, the dc link comprises two identical film capacitors ($C_{\rm dc1} = C_{\rm dc2} = C_f$) connected in series, and the middle point is connected to one converter leg through the filter inductor L_r. By appropriate modulation of this phase leg, the ripple power can be absorbed by the dc-link film capacitors. The other converter

leg in the full-bridge should be modulated in such a way that the grid current is sinusoidal, where the phase angle of the grid current is determined by the reactive power requirement.

For mode I or II, the single-phase input power, $p_{\rm in}$, where instantaneous power of the grid inductor L_s is neglected to simplify the analysis, is expressed as

$$p_{\rm in} = V_s I_s + V_s I_s \cos(2\omega t) = p_{\rm dc} + p_{\rm ac} \tag{1}$$

where V_s and I_s are the rms values of the grid voltage and current, respectively, and ω is the angular frequency. The input power of the OBC includes a dc power component, $p_{\rm dc}$, which is fed to the dc–dc converter, and an ac ripple power component, $p_{\rm ac}$, caused by the second-order harmonic components, which need to be decoupled by the APD circuit. To do this, the upper and lower capacitor voltages, v_{c1} and v_{c2} should be controlled to be sinusoidal with an offset value that is equal to a half of the dc-link voltage ($V_{\rm dc}/2$), which can be expressed as [19]

$$v_{c1}(t) = \frac{V_{\rm dc}}{2} + V_c \sin(\omega t + \phi) \tag{2}$$

$$v_{c1}(t) = \frac{V_{\rm dc}}{2} - V_c \sin(\omega t + \phi). \tag{3}$$

From (2) and (3), the upper capacitor current, $\mathrm{i_{c1}(t)}$, and lower capacitor current, $\mathrm{i_{c2}(t)}$, can be derived as

$$i_{\rm c1}(t) = \omega C_f V_c \cos(\omega t + \phi) \tag{4}$$

$$i_{\rm c2}(t) = -\omega C_f V_c \cos(\omega t + \phi), \tag{5}$$

Where C_f is the capacitance of $C_{\rm dc1}$ and $C_{\rm dc2}$.

From (2) to (5), the instantaneous power of the APD circuit is derived as

$$\begin{aligned} p_{\rm APD}(t) &= i_{c1}(t)\, v_{c1}(t) + i_{c2}(t)\, v_{c2}(t) \\ &= \omega C_f V_c^2 \sin(2\omega t + 2\phi). \end{aligned} \tag{6}$$

By setting the time-varying term in (1) equal to (6), the amplitude, and phase angle, of the capacitor voltage reference are determined as

$$V_c = \sqrt{\frac{V_s I_s}{\omega C_f}} \tag{7}$$

$$\phi = -\frac{\pi}{4} \text{or} \phi = \frac{3\pi}{4}. \tag{8}$$

By controlling the capacitor voltage to follow the reference given by (7) and (8), the ripple power can be absorbed by the two decoupling capacitors. As a result, the required dc-link capacitance for keeping the dc-link voltage constant is reduced significantly.

To examine the capacitance reduction due to the APD circuit, it is assumed that the ripple power in the input inductor, $L_{\rm s}$, and filter inductor, L_r, is neglected. In this case, the ripple power of the APD circuit is the highest at $V_{\rm c} = V_{\rm dc}/2$. Then, the capacitance, C_f, of the filter capacitor is obtained as

$$C_f = \frac{4V_s I_s}{V_{\rm dc}^2 \omega} = \frac{4P_{\rm in}}{V_{\rm dc}^2 \omega}. \tag{9}$$

Here, the equivalent capacitance at the dc link, $C_{\rm eq}$, is defined by

$$C_{\rm eq} = \frac{C_f}{2} = \frac{2P_{\rm in}}{V_{\rm dc}^2 \omega} \tag{10}$$

where $P_{\rm in}$ is the amplitude of the input ripple power.

In a 60-Hz system with a dc-link voltage of 350 V, the required capacitance per input power is about 43.15 μF/kW. Considering the practical condition, the capacitance C_f is selected as 100 μF.

In a conventional full-bridge ac–dc converter [9], the dc-link capacitance is

$$C = \frac{P_{\rm in}}{\omega V_{\rm dc} \Delta V_{\rm dc}}. \tag{11}$$

If the peak-to-peak ripple voltage, $\Delta V_{\rm dc}$ is set to 10 V, the required capacitance is about 1.5 mF.

Since the APD circuit is operated in a continuous mode, the filter inductor, $L_{\rm r}$ consumes some reactive power. To account for this effect, a cancellation coefficient, α, is used, which is defined as [20]

$$\alpha = \omega^2 L_r C_f. \tag{12}$$

From (12), the filter inductance can be determined. It is noticed that the cancelation coefficient should be kept as small as possible to minimize reactive power consumption. However, an inductor that is too small leads to excessively high switching ripple currents, which increase the current stress. The control bandwidth of the APD is also affected by the cancelation factor. Considering these conditions, the cancelation coefficient is selected as 0.075, which results in a filter inductance of 1 mH.

B. Bidirectional Buck–Boost DC–DC Converter

Since the dc-link voltage is kept constant while the HV battery needs to operate in a wide voltage range, the dc–dc converter has to be able to cover this voltage range [21]–[24]. The dc–dc converter consists of four switches (S_5–S_8), output capacitor ($C_{\rm HV}$), and inductor ($L_{\rm HV}$), where the direction of the power flow between the dc link and HV battery is controlled by the switches and the inductor. Depending on the voltage level of the HV battery, the converter is operated as buck, boost, or buck–boost converters by controlling the duty cycle d of the switches (S_5, S_6, S_7, S_8), as shown in Table II.

In charging mode, when the HV battery voltage is lower than the dc-link voltage, S_7 is fully turned ON and S_8 is fully turned OFF. The converter works as a buck converter, and S_5 and S_6 are controlled by d, and $1-d$, respectively. When the HV battery voltage is higher than the dc-link voltage, $\mathrm{S_5}$ is fully turned ON and $\mathrm{S_6}$ is fully turned OFF, and the converter functions as a boost converter. S_8 and S_7 are controlled by d and $1-d$, respectively. When the HV battery voltage is close to the dc-link voltage, S_5 and S_8 are controlled by d, and S_6 and S_7 are controlled by $1-d$. In this case, the converter is operated as a buck–boost converter. For discharging mode, a similar operating principle is applied to control the energy from the HV battery to the dc link. To further reduce the switching loss, a soft-switching technique is applied by changing the switching frequency, $f_{\rm sw}$, so that the switches can be turned ON with zero-voltage switching (ZVS)

TABLE II
OPERATING CONDITIONS OF THE BUCK-BOOST CONVERTER

Direction of the power	Operation modes	Duty cycle (0 →1)			
		S_5	S_6	S_7	S_8
$V_{dc} \rightarrow V_{HV}$ (Charging HV battery)	Buck ($250V \le V_{HV} \le 320V$)	d	$1-d$	1	0
	Buck-boost ($320V \le V_{HV} \le 380V$)	d	$1-d$	$1-d$	d
	Boost ($380V \le V_{HV} \le 430V$)	1	0	$1-d$	d
$V_{HV} \rightarrow V_{dc}$ (Discharging HV battery)	Buck ($380V \le V_{HV} \le 430V$)	1	0	d	$1-d$
	Buck-boost ($320V \le V_{HV} \le 380V$)	$1-d$	d	d	$1-d$
	Boost ($250V \le V_{HV} \le 320V$)	$1-d$	d	1	0

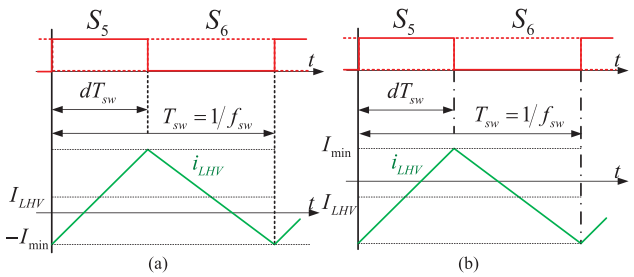

Fig. 5. Waveform of inductor current in buck mode. (a) $I_{LHV} \ge 0$. (b) $I_{LHV} < 0$.

[21], [25]–[28]. The direction of the inductor current i_{LHV} from the dc link to the HV battery is defined as positive, and the opposite direction is negative. The ZVS of the switches can be achieved by controlling the direction of this current.

Fig. 5 shows the waveform of the inductor current in buck mode. For the dc-link side, the inductor current i_{LHV} should be positive while turning OFF S_5 and S_8. On the HV battery side, the inductor current i_{LHV} should be negative while turning OFF S_4 and S_7. Also, the absolute value of the inductor current should be greater than a certain value I_{min} so that the output capacitor of the MOSFET (C_{oss}) is charged or discharged fully during the deadtime, t_{dead}. Since the inductor current varies depending on the operating conditions, the switching frequency needs to be adaptively adjusted to achieve the optimal switching frequency, which is listed in Table III. The switching frequency is calculated from the measured dc-link voltage, HV battery voltage, and the average measured inductor current I_{LHV}. I_{min} can be calculated by

$$I_{\min} = \frac{2C_{oss}\max(V_{dc}, V_{HV})}{t_{dead}}. \quad (13)$$

The dc–dc converter needs to operate in both buck and boost modes, so the inductor should be designed to cover both the

TABLE III
OPTIMAL SWITCHING FREQUENCY OF THE DC–DC CONVERTER

Operating modes	$I_{LHV} \ge 0$	$I_{LHV} < 0$
Buck	$\frac{V_{dc}V_{HV} - V_{HV}^2}{V_{dc}2L_{HV}(I_{LHV} + I_{min})}$	$\frac{V_{dc}V_{HV} - V_{HV}^2}{V_{dc}2L_{HV}(I_{LHV} - I_{min})}$
Buck-boost	$\frac{V_{dc}V_{HV}}{(V_{dc}+V_{HV})2L_{HV}(I_{LHV} + I_{min})}$	$\frac{V_{dc}V_{HV}}{(V_{dc}+V_{HV})2L_{HV}(I_{LHV} - I_{min})}$
Boost	$\frac{V_{dc}V_{HV} - V_{dc}^2}{V_{HV}2L_{HV}(I_{LHV} + I_{min})}$	$\frac{V_{dc}V_{HV} - V_{dc}^2}{V_{HV}2L_{HV}(I_{LHV} - I_{min})}$

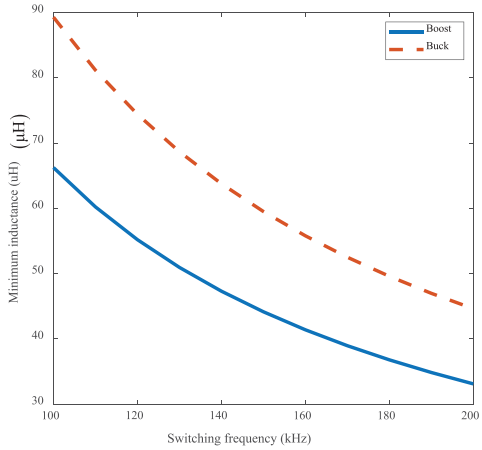

Fig. 6. Minimum inductance for buck–boost dc–dc converter.

cases [29]–[31]. Fig. 6 shows the minimum inductance versus the switching frequency, which is limited to 100–200 kHz. Therefore, the inductance of L_{HV} is selected as 100 μH.

C. LV Charging Circuits

The LV battery is charged from the HV battery through the HP-LVC or LP-LVC depending on the operating conditions. Since the LV battery is mostly charged through the HP-LVC, a 1-kW power rating is considered, which includes the dc–dc stage of the OBC and the resonant LLC converter. In this case, four switches of the ac–dc stage are used as the primary side of the resonant converter. The LP-LVC is operated only during the HV battery charging. When the vehicle is connected to the grid, the shared components need to be involved in an APD circuit. During this period, LV loads will still consume power. The worst case happens when the LV battery is depleted while the HV battery is being charged. To take this situation into account, a 500-W LP-LVC is added which is composed of a half-bridge LLC converter. The consumed power of the LV loads is not considerable during HV battery charging, so the LP-LVC can use the same transformer core and secondary side of the HP-LVC.

In the HP-LVC, the resonant tank consists of an inductor L_{r1} and capacitor C_{r1} connected in series. A square wave voltage, v_{HP_pri}, is generated by a group of switches (S_1, S_2) and (S_3, S_4) with a duty cycle of 0.5. The LV battery voltage is controlled by changing the frequency of v_{HP_pri}. The operation of the resonant converter is characterized by the ratio between the switching frequency f_{sw}, and the resonant frequency

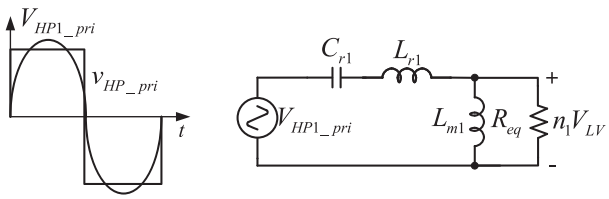

Fig. 7. AC equivalent circuit of the resonant converter for LV charging.

TABLE IV
PARAMETERS OF RESONANT LLC CONVERTERS FOR LOW-VOLTAGE CHARGING CIRCUITS

Parameters	LP-LVC	HP-LVC
Transformer turn ratio	14:1	28:1
Resonant inductance L_r	34 μH	68 μH
Resonant capacitance C_r	37 nF	74 nF
Magnetizing inductance	120 μH	250 μH
Resonant frequency f_r	100 kHz	100 kHz
Switching frequency range	90 kHz – 150 kHz	

$f_{r1}= 1/(2\pi\sqrt{L_{r1}C_{r1}})$. The ac equivalent circuit of the LLC converter based on the fundamental harmonic approximation method is shown in Fig. 7, where v_{HP1_pri} is the fundamental component of v_{HP_pri} [32]–[34]. The ac equivalence of the load resistance is defined as

$$R_{\rm eq} = n_1^2 \frac{8V_{\rm LV}^2}{\pi^2 P_{\rm H-LVC}} \tag{14}$$

where $V_{\rm LV}$ and $P_{\rm H-LVC}$ are the voltage and the power of the HP-LVC, respectively. The transformer turns ratio, n_1, is determined using the dc-link voltage and the nominal voltage of the LV battery, $V_{\rm LV\_nor}$

$$n_1 = \frac{V_{\rm dc}}{V_{\rm LV\_nor}}. \tag{15}$$

Based on the characteristic impedance, $Z_{r1} = \sqrt{L_{r1}/C_{r1}}$, the quality factor Q is defined as

$$Q = \frac{Z_{r1}}{R_{\rm eq}}. \tag{16}$$

Then, the dc voltage gain, $M_{\rm FHA}$ is obtained as follows:

$$M_{\rm FHA} = \frac{n_1 V_{\rm LV}}{V_{\rm dc}} \frac{1}{\sqrt{\left(1 + L_n - \frac{L_n}{f_n^2}\right) + Q^2\left(f_n - \frac{1}{f_n}\right)^2}} \tag{17}$$

where $f_n = f_{\rm sw}/f_{r1}$ is the normalized switching frequency, and $L_n = L_{\rm m1}/L_{r1}$ is the inductance ratio.

In the LP-LVC, the same procedure can be applied to calculate the parameters except that the transformer turns ratio and the voltage gain are reduced by half due to the half-bridge structure of the resonant converter. The parameters designed for the HP-LVC and LP-LVC are listed in Table IV. Fig. 8 shows the voltage gain versus normalized frequency for different operating conditions. In this case, since the dc-link voltage is controlled by the dc–dc converter, the input voltage of the HP-LVC is kept constant. Therefore, the switching frequency is optimal and close to the resonant frequency of 100 kHz, as shown in Fig. 8(a).

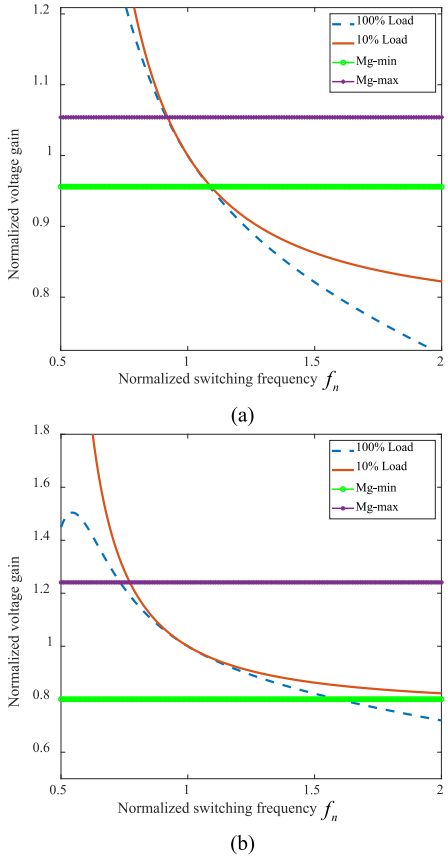

Fig. 8. Voltage gains of the low-voltage charging circuits. (a) High-power low-voltage charging circuit. (b) Low-power low-voltage charging circuit.

For the LP-LVC, the input voltage varies depending on the HV battery voltage. Therefore, the switching frequency needs to have a wide range to control the output power. In light load conditions, the switching frequency should be high to regulate the output voltage, which affects the power losses. However, it should be noted that the LP-LVC is operated with only a heavy load when the LV battery is depleted, so the switching frequency range can be reduced.

Fig. 9 shows the winding configuration of the transformer for the LV charging circuit. The selection of the core size and material is done according to this condition along with the power density target and the available airflow, where the TDK-Epcos PQ50/50 PC95 ferrite core is used. The 360 strands Litz wire with a single strand diameter of 0.06 mm is used for the primary winding, which can reduce the ac losses due to skin and proximity effect. The secondary one is made with copper band 20 × 0.5 mm.

D. Overall Control of Proposed OBC

A detailed control block diagram of the proposed OBC is shown in Fig. 10. To improve the dynamic response, the controller gains are tuned finely by a trial and error method. When

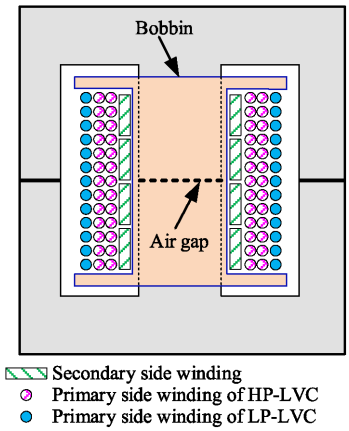

Fig. 9. Winding configuration of the transformer.

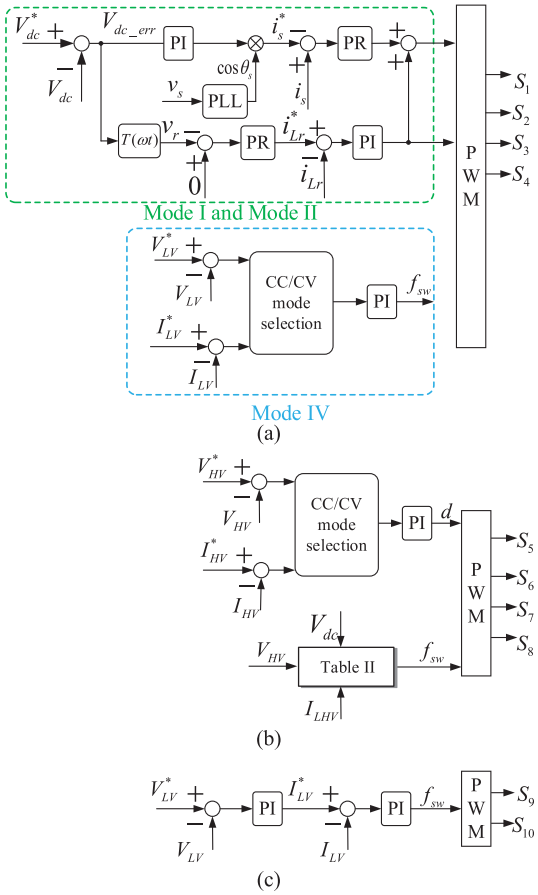

Fig. 10. Overall control block diagram of the proposed onboard battery charger. (a) AC–DC converter. (b) DC–DC converter. (c) Half-bridge LLC converter.

the OBC is connected to the grid (mode I or mode II), the dc-link voltage and grid current are controlled by the ac–dc converter. Then, the voltage references for C_{dc1} and C_{dc2} can be determined by (7) and (8). However, since these values are dependent on the system parameters, it is very difficult to achieve perfect power decoupling. Therefore, the closed-loop control is applied to achieve the APD capability. The dynamic model of the ac–dc converter with APD function and its controller design can be referred to in [7]. The target of the APD circuit is to control the APD capacitor voltages to be sinusoidal as given in (2) and (3), which contains only the fundamental frequency component. Since the dc-link voltage error consists of the second-order harmonic component, it needs to be transformed into a fundamental frequency frame for controlling the APD circuit by using the transformation matrix $T(\omega t)$ [13], [14]. Then, a proportional-resonant controller is adopted to control the dc-link voltage ripple to zero. Also, the inductor current is regulated using a PI controller, as shown in Fig. 10(a). For mode II, the controllers are the same as those of Fig. 10(a) except that the signs of the dc-link voltage and the grid current are reversed. When the vehicle is running, the voltage and current of the LV battery are controlled by varying the switching frequencies of the switches (S_1, S_2) and (S_3, S_4).

The voltage and current of the HV battery are controlled by the dc–dc converter. Depending on the voltage levels of the HV battery and dc link, the dc–dc converter can be operated as a buck, buck–boost, or boost converter by varying the duty cycle to control the current and voltage of the HV battery. To ensure ZVS turn-ON of the switches, the inductor current is measured to calculate the optimal switching frequency, as shown in Fig. 10(b).

When the LV battery needs to be charged during HV battery charging, the half-bridge LLC is activated. The voltage and current of the LV battery are controlled by the switching frequencies of S_9 and S_{10}, as shown in Fig. 10(c). When the LV battery is fully charged, the operation mode is changed to G2V.

IV. Comparative Analysis

In this section, the cost, and volume of the proposed battery charger are evaluated and compared with those of a conventional OBC with a cascaded connection of LV charging circuit, where large film capacitor banks are used at the dc link of the ac–dc converter, as shown in Fig. 11. The volume is estimated based on the dimensions provided in the datasheets, where those of the transformer and inductor windings are neglected [35], [36]. The volume comparison is shown in Fig. 12(a). The overall volume of the proposed charger is reduced by 52.3% compared with that of the conventional one. In addition, with the proposed LV charger with APD function, the overall cost of the proposed circuit is decreased by 46.9% due to the reduction of the dc-link capacitor, as shown in Fig. 12(b).

In order to demonstrate the advantages of the proposed OBC, some features are investigated with other converter topologies [13], [15], [16], [37], [38], which are listed in Table V. Among these topologies, the onboard reconfigurable battery charger [38] has the lowest number of switches. However, the large dc-link capacitance is required, and it is impossible to charge the LV battery when the HV battery is charged. Although a bidirectional EV charger in [37] can reduce the dc-link capacitance, the sinusoidal charging current may be problems not only for the lifetime of the traction battery but also for charging the LV battery during HV charging mode. The multifunctional OBC [13] can achieve APD capability, but it requires a higher

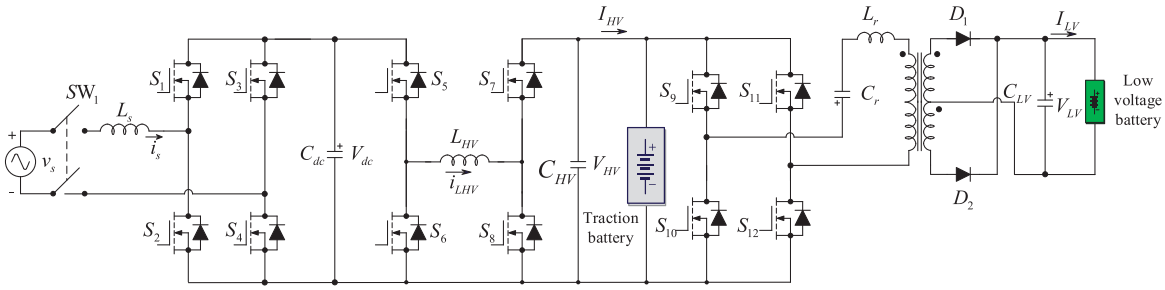

Fig. 11. Conventional onboard battery charger with the cascaded connection of low-voltage charging circuit.

TABLE V
COMPARISON OF DIFFERENT ONBOARD BATTERY CHARGERS

Description		[13]	[15]	[16]	[37]	[38]	Proposed
No. of switches		14	11	11	8	6	10
No. of diodes		0	9	9	0	2	2
No. of inductors		3	5	5	4	3	5
No. of transformers		1	1	1	1	1	1
Galvanic isolation		Isolated	Non-isolated	Isolated	Isolated	Non-isolated	Non-isolated
Control complexity		Simple	Medium	High	High	Simple	Medium
Switching frequency		10 kHz	150 kHz	100 kHz	50 kHz	20 kHz – 40 kHz	100 kHz
V2G		Yes	No	No	Yes	Yes	Yes
H2L		Yes	Yes	Yes	No	Yes	Yes
GH2L		No	Yes	Yes	No	No	Yes
APD capability		Yes	No	No	Yes	No	Yes
Peak efficiency (%)	G2V	92.6	97.3	93.5	95.7	N.A.	96.1
	V2G	91.8	N.A.	N.A.	95.4	N.A.	95.0
	H2L	89.2	93.1	95.0	N.A.	N.A.	95.2

Yes: capable *No: incapable* *N.A.: not available*

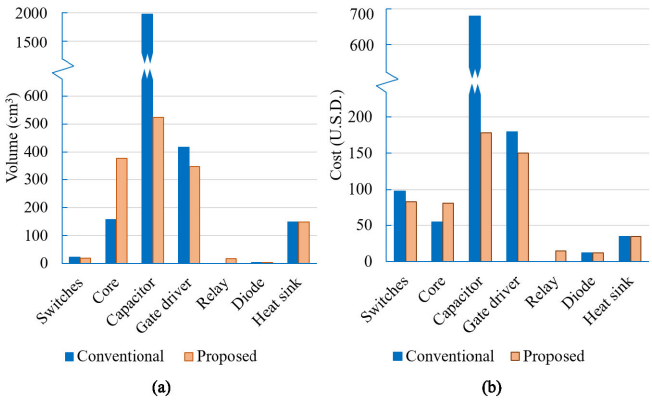

Fig. 12. Comparison of main components. (a) Volume. (b) Cost.

number of devices. Also, the LV battery cannot be charged when the traction battery is charged. In addition, with integrated charging circuits [15], [16], LV and HV batteries can be charged simultaneously, but unidirectional power flow and large dc-link capacitance are main disadvantages. Consequently, the proposed multifunctional OBC clearly stands out from the existing topologies since some devices are used in common for not only power decoupling but also LV battery charging, which results in a more cost-effective system. Furthermore, the efficiency of the proposed OBC is similar to that of the existing topologies.

V. EXPERIMENTAL RESULTS

To verify the effectiveness of the proposed circuit, a 2-kW prototype has been built, as shown in Fig. 13. A TMS320F28377 digital signal processor is used for the main controller. The system parameters are listed in Table VI. The OBC is designed using SiC MOSFETs, which have very low switching losses and ON-resistances. The output terminal of the OBC is connected to the PWM converter, which is used as a controllable voltage source. For the LV charging circuit, the output terminal is connected to the load resistor.

Fig. 14 shows the operation of the proposed battery charger in mode I at rated condition. In Fig. 14(a), the dc-link voltage ripple is kept constant when the APD is applied to filter out the second-order ripple power. The input current is controlled to be sinusoidal at unity power factor. The upper and lower capacitor

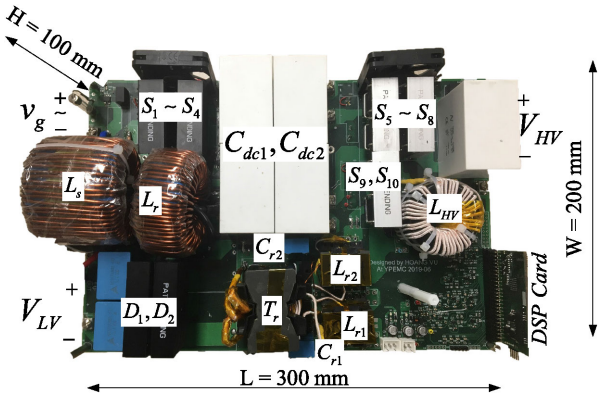

Fig. 13. A 2-kW onboard battery charger prototype.

TABLE VI
SPECIFICATIONS OF THE PROPOSED CONVERTER

Parameter	Specification
Switches S_1 - S_4	C3M0065090D
Switches S_5 - S_{10}	E3M0120090D
Diodes D_1 - D_4	DSSK 80-0045B
Capacitors C_{dc1} - C_{dc2}	C4AQCBW5500A3OJ
Grid inductor L_s	1.8 mH
Filter inductor L_r	1 mH
Buck-boost inductor L_{HV}	100 µH.
Transformer core T_r	PQ50/50 TDK PC95

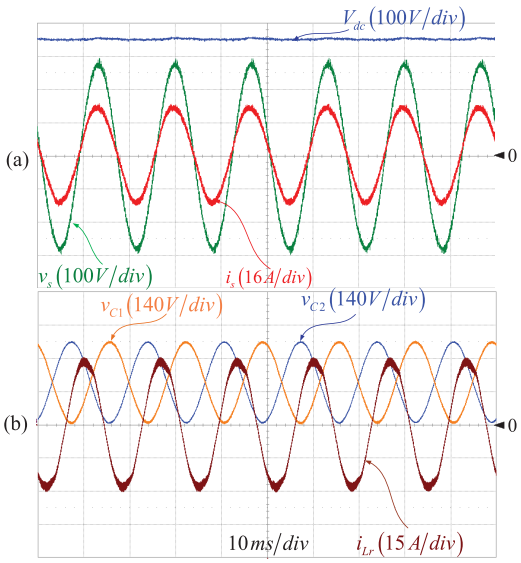

Fig. 14. Operation of the ac–dc converter in Mode I at rated power condition.

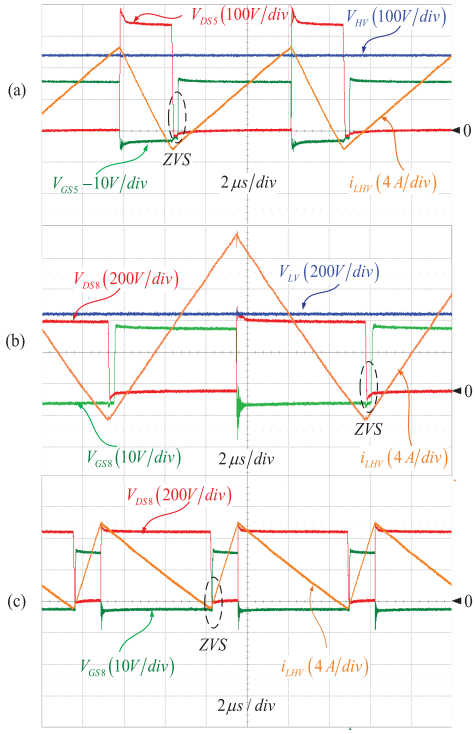

Fig. 15. Operation of the dc–dc converter in mode I at rated power condition. (a) Buck mode. (b) Buck–boost mode. (c) Boost mode.

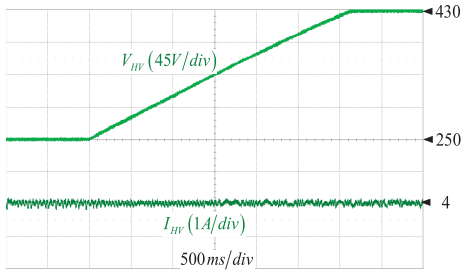

Fig. 16. Transient performance of the onboard battery charger in G2V mode.

voltages are well controlled as discussed in the theoretical results, which is shown in Fig. 14(b). The inductor current is also kept being sinusoidal.

The operation of the nonisolated dc–dc converter is shown in Fig. 15. The converter can be operated in buck, buck–boost, and boost modes according to the HV battery voltage, as shown in Fig. 15(a)–(c), respectively. The switching frequency varies depending on the operating points. Therefore, the ZVS turn-ON is achieved. In addition, the inductor current ripple in buck–boost mode is much higher than those in buck and boost modes due to lower switching frequency.

Fig. 16 shows the transient performance of the OBC when the voltage of HV battery increases from 250 to 430 V. The LV battery current is controlled at 4 A. Fig. 17 shows the performance of the system in mode II, where the proposed charger acts as a dc–ac inverter. In this case, the discharging current of 3 A is controlled by the dc–dc converter. Even though the power flow is reversed, the APD circuit still operates to keep the dc-link voltage constant at 350 V. The input current and capacitor voltages are controlled to be sinusoidal.

The measured efficiency of the OBC is illustrated in Fig. 18. In mode I, a peak efficiency of 96.1% is achieved when the OBC operates at rated conditions. In mode II, the peak efficiency is 95.0%. The system efficiency varies depending on the load

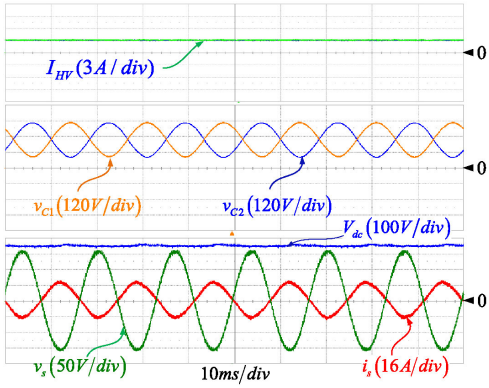

Fig. 17. Operation of the onboard battery charger in mode II.

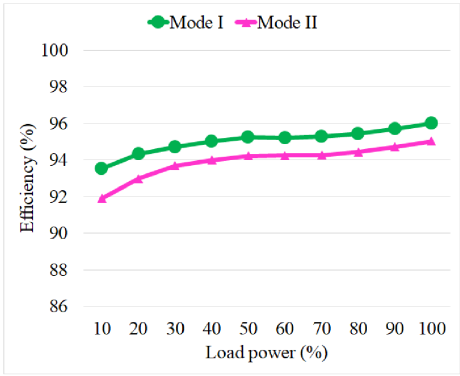

Fig. 18. Efficiency of the onboard battery charger in mode I and II.

condition related to the state of charge of the battery. At a light load condition, the system efficiency drops due to high current stresses in S_3 and S_4 resulting from the operation of the APD circuit.

Fig. 19 shows the performance of the OBC in mode III, where the dc–dc converter and HP-LVC are used to charge the LV battery. The LLC resonant converter is tested under the maximum and minimum voltage gain conditions. The dc-link voltage is kept constant, so the switching frequency of the HP-LVC can be kept at the resonant frequency of 100 kHz. In both cases of voltage gain, ZVS turn-ON of the switches is achieved.

Fig. 20 shows the operation of the OBC in mode IV, where the OBC and LP-LVC are operated at the same time. At the lowest output voltage of 250 V, the switching frequency is 90 kHz, which is below the series resonant frequency to achieve the maximum voltage gain, as shown in Fig. 20(a). In Fig. 20(b), when the HV battery voltage increases to 350 V, the resonant current and voltage are almost sinusoidal, where the switching frequency is equal to the series resonant frequency of 100 kHz. In light load conditions, the switching frequency is increased to 145 kHz to reach the minimum voltage gain. Thus, in this case, the OBC controls the HV battery voltage at 430 V and the LP-LVC controls the LV battery current at 4 A, as shown in Fig. 20(c). ZVS is also realized in all conditions. The measured

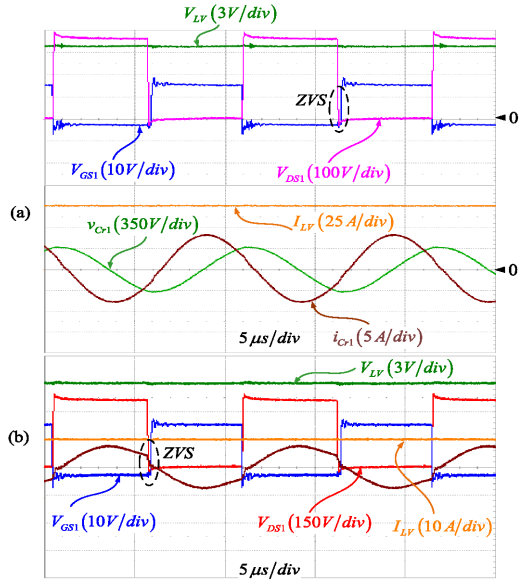

Fig. 19. Operation of the onboard battery charger in mode III. (a) $V_{\mathrm{LV}} = 13$ V and $I_{\mathrm{LV}} = 76$ A. (b) $V_{\mathrm{LV}} = 12$ V and $I_{\mathrm{LV}} = 10$ A.

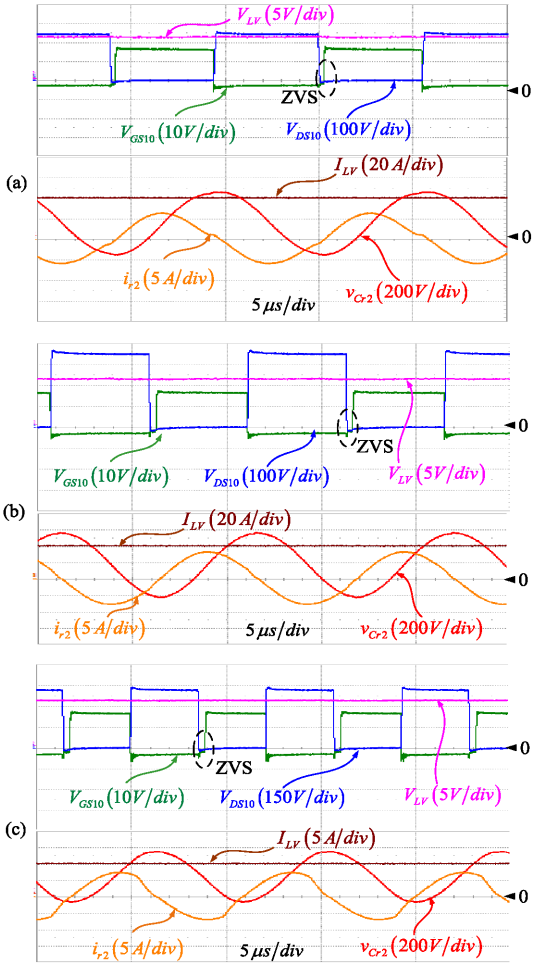

Fig. 20. Operation of the OBC in mode IV. (a) $V_{\mathrm{HV}} = 250$ V and $I_{\mathrm{LV}} = 40$ A. (b) $V_{\mathrm{HV}} = 350$ V and $I_{\mathrm{LV}} = 40$ A. (c) $V_{\mathrm{HV}} = 430$ V and $I_{\mathrm{LV}} = 4$ A.

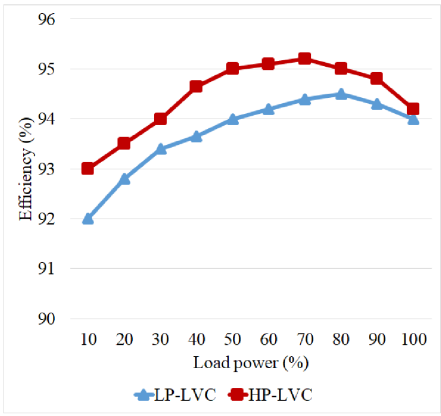

Fig. 21. Measured efficiency of the low-voltage charging circuit.

efficiency of the LV charging circuit is illustrated in Fig. 21, where the highest efficiencies of the HP-LVC and LP-LVC are 95.3% and 94.5%, respectively.

VI. Conclusion

A novel multifunctional battery charger for EVs has been proposed in this article. The proposed OBC can realize dual functions, which reduces the number of circuit components. When a vehicle is connected to the grid to charge or discharge the HV battery, the LV charging circuit is operated as an APD circuit to absorb the second-order ripple power at the dc link. When the vehicle is running, the LV charging circuit is operated as an LLC resonant converter to charge the LV battery from the HV battery. With the proposed topology, the LV battery charging circuit is utilized to achieve the APD function instead of bulky capacitor banks. Therefore, small film capacitors can be used without adding any switch, heat sink, or corresponding gate circuit. As a result, the volume and cost can be reduced by 52.3% and 46.9%, respectively, compared with the conventional method. In addition, the LV battery can be charged from both the HV battery and the grid utility. The feasibility of the proposed OBC has been verified for a 2-kW SiC-based prototype in the laboratory, where the highest efficiencies of the OBC and LV charger were 96.1% and 95.3%, respectively.

References

[1] B. Bilgin *et al.*, "Making the case for electrified transportation," *IEEE Trans. Transp. Electrific.*, vol. 1, no. 1, pp. 4–17, Jun. 2015.
[2] L. Xue, Z. Shen, D. Boroyevich, P. Mattavelli, and D. Diaz, "Dual active bridge-based battery charger for plug-in hybrid electric vehicle with charging current containing low frequency ripple," *IEEE Trans. Power Electron.*, vol. 30, no. 12, pp. 7299–7307, Dec. 2015.
[3] S. Wang, X. Ruan, K. Yao, S.-C. Tan, Y. Yang, and Z. Ye, "A flicker-free electrolytic capacitorless AC–DC led driver," *IEEE Trans. Power Electron.*, vol. 27, no. 11, pp. 4540–4548, Nov. 2012.
[4] H. Wang and F. Blaabjerg, "Reliability of capacitors for DC-link applications in power electronic converters–An overview," *IEEE Trans. Ind. Appl.*, vol. 50, no. 5, pp. 3569–3578, Sep. 2014.
[5] M. A. Vitorino, R. Wang, M. B. D. R. Correa, and D. Boroyevich, "Compensation of DC-link oscillation in single-phase-to-single-phase VSC/CSC and power density comparison," *IEEE Trans. Ind. Appl.*, vol. 50, no. 3, pp. 2021–2028, May 2014.
[6] Y. Tang, F. Blaabjerg, and P. C. Loh, "Decoupling of fluctuating power in single-phase systems through a symmetrical half-bridge circuit," *IEEE Trans. Power Electron.*, vol. 30, no. 4, pp. 1855–1865, Mar. 2015.
[7] Y. Tang, Z. Qin, F. Blaabjerg, and P. C. Loh, "A dual voltage control strategy for single-phase PWM converters with power decoupling function," *IEEE Trans. Power Electron.*, vol. 30, no. 12, pp. 7060–7071, Dec. 2015.
[8] Y. Sun, Y. Liu, M. Su, W. Xiong, and J. Yang, "Review of active power decoupling topologies in single-phase systems," *IEEE Trans. Power Electron.*, vol. 31, no. 7, pp. 4778–4794, Jul. 2016.
[9] R. Chen, Y. Liu, and F. Z. Peng, "DC capacitor-less inverter for single-phase power conversion with minimum voltage and current stress," *IEEE Trans. Power Electron.*, vol. 30, no. 10, pp. 5499–5507, Oct. 2015.
[10] S. Kim and F. Kang, "Multifunctional on-board battery charger for plug-in electric vehicles," *IEEE Trans. Ind. Electron.*, vol. 62, no. 6, pp. 3460–3472, Jun. 2014.
[11] R. Hou and A. Emadi, "Applied integrated active filter auxiliary power module for electrified vehicles with single-phase onboard chargers," *IEEE Trans. Power Electron.*, vol. 32, no. 3, pp. 1860–1871, Mar. 2017.
[12] R. Hou and A. Emadi, "A primary full-integrated active filter auxiliary power module in electrified vehicles with single-phase onboard chargers," *IEEE Trans. Power Electron.*, vol. 32, no. 11, pp. 8393–8405, Nov. 2017.
[13] H. V. Nguyen, D.-D. To, and D.-C. Lee, "Onboard battery chargers for plug-in electric vehicles with dual functional circuit for low-voltage battery charging and active power decoupling," *IEEE Access*, vol. 6, no. 1, pp. 70212–70222, Oct. 2018.
[14] H. V. Nguyen, S. Lee, and D. C. Lee, "Reduction of dc-link capacitance in single-phase non-isolated onboard battery chargers," *J. Power Electron.*, vol. 19, no. 2, pp. 394–402, Mar. 2019.
[15] D.-H. Kim, M.-J. Kim, and B.-K. Lee, "An integrated battery charger with high power density and efficiency for electric vehicles," *IEEE Trans. Power Electron.*, vol. 32, no. 6, pp. 4553–4565, Jun. 2017.
[16] Y.-S. Kim, C.-Y. Oh, W.-Y. Sung, and B. K. Lee, "Topology and control scheme of OBC-LDC integrated power unit for electric vehicles," *IEEE Trans. Power Electron.*, vol. 32, no. 3, pp. 1731–1743, Mar. 2017.
[17] Y. Tang, J. Lu, B. Wu, S. Zou, W. Ding, and A. Khaligh, "An integrated dual-output isolated converter for plug-in electric vehicles," *IEEE Trans. Veh. Technol.*, vol. 67, no. 2, pp. 966–976, Feb. 2018.
[18] *Electric Vehicle and Plug In Hybrid Electric Vehicle Conductive Charger Coupler*, SAE International, Standard Recommended Practice J1772, Jan. 2010.
[19] Y. Tang and F. Blaabjerg, "A component-minimized single-phase active power decoupling circuit with reduced current stress to semiconductor switches," *IEEE Trans. Power Electron.*, vol. 30, no. 6, pp. 2905–2910, Jun. 2015.
[20] H. Li, K. Zhang, H. Zhao, S. Fan, and J. Xiong, "Active power decoupling for high-power single-phase PWM rectifiers," *IEEE Trans. Power Electron.*, vol. 28, no. 3, pp. 1308–1319, Mar. 2013.
[21] Z. Yu, H. Kapels, and K. F. Hoffmann, "High efficiency bidirectional DC-DC converter with wide input and output voltage ranges for battery systems," in *Proc. Int. Exhib. Conf. Power Electron. Intell. Motion Renewable Energy Energy Manage*, 2015, pp. 19–21.
[22] Jingquan Chen, D. Maksimovic, and R. Erickson, "Buck-boost PWM converters having two independently controlled switches," in *Proc. IEEE 32nd Annu. Power Electron. Specialists Conf.*, 2001, pp. 736–741.
[23] C. Restrepo, J. Calvente, A. Cid-Pastor, A. El Aroudi, and R. Giral, "A noninverting buck-boost DC-DC switching converter with high efficiency and wide bandwidth," *IEEE Trans. Power Electron.*, vol. 26, no. 9, pp. 2490–2503, Sep. 2011.
[24] P.-C. Huang, W.-Q. Wu, H.-H. Ho, and K.-H. Chen, "Hybrid buck-boost feedforward and reduced average inductor current techniques in fast line transient and high-efficiency buck-boost converter," *IEEE Trans. Power Electron.*, vol. 25, no. 3, pp. 719–730, Mar. 2010.
[25] Z. Yu, H. Kapels, and K. F. Hoffmann, "Extreme high efficiency non-inverting buck-boost converter for energy storage systems," in *Proc. Int. Exhib. Conf. Power Electron. Intell. Motion Renewable Energy Energy Manage.*, 2016, pp. 202–209.
[26] Z. Yu, H. Kapels, and K. F. Hoffmann, "A novel control concept for high-efficiency power conversion with the bidirectional non-inverting buck-boost converter," in *Proc. 18th Eur. Conf. Power Electron. Appl.*, 2016, pp. 1–10.
[27] S. Waffler and J. W. Kolar, "A novel low-loss modulation strategy for high-power bidirectional buck + boost converters," *IEEE Trans. Power Electron.*, vol. 24, no. 6, pp. 1589–1599, Jun. 2009.
[28] H. S. Lee and J. J. Yun, "High-efficiency bidirectional buck-boost converter for photovoltaic and energy storage systems in a smart grid," *IEEE Trans. Power Electron.*, vol. 34, no. 5, pp. 4316–4328, May 2019.

[29] J. Hagedom, "Basic calculations of a 4 switch buck-boost power stage," *Appl. Rep.*, Texas Instruments, Dallas, TX, USA, 2018.
[30] B. Hauke, "Basic calculation of a boost converter's power stage," Appl. Rep., Texas Instruments, Dallas, TX, USA, 2009.
[31] B. Hauke, "Basic calculation of a buck converter's power stage," *Appl. Rep.*, Texas Instruments, Dallas, TX, USA, 2015.
[32] J. Deng, S. Li, S. Hu, C. C. Mi, and R. Ma, "Design methodology of LLC resonant converters for electric vehicle battery chargers," *IEEE Trans. Veh. Technol.*, vol. 63, no. 4, pp. 1581–1592, May 2014.
[33] R. Beiranvand, B. Rashidian, M. R. Zolghadri, and S. M. Hossein Alavi, "A design procedure for optimizing the LLC resonant converter as a wide output range voltage source," *IEEE Trans. Power Electron.*, vol. 27, no. 8, pp. 3749–3763, Aug. 2012.
[34] A. Safaee, M. Karimi-Ghartemani, P. K. Jain, and A. Bakhshai, "Time-domain analysis of a phase-shift-modulated series resonant converter with an adaptive passive auxiliary circuit," *IEEE Trans. Power Electron.*, vol. 31, no. 11, pp. 7714–7734, Nov. 2016.
[35] Digi-Key Electronics, 2019. [Online]. Available: http://www.digikey.com/
[36] "Mouser Electronics," 2019. [Online]. Available: http://www.mouser.com/
[37] M. Kwon and S. Choi, "An electrolytic capacitorless bidirectional EV charger for V2G and V2H applications," *IEEE Trans. Power Electron.*, vol. 32, no. 9, pp. 6792–6799, Sep. 2017.
[38] J. G. Pinto, V. Monteiro, H. Goncalves, and J. L. Afonso, "Onboard reconfigurable battery charger for electric vehicles with traction-to-auxiliary mode," *IEEE Trans. Veh. Technol.*, vol. 63, no. 3, pp. 1104–1116, Mar. 2014.

Hoang Vu Nguyen (Member, IEEE) received the B.S. degree from Can Tho University, Can Tho, Vietnam, in 2012, the Ph.D. degree from Yeungnam University, Gyeongsan, South Korea, in 2019, both in electrical engineering.

He was a Visiting Ph.D. Student in the Department of Energy Technology, Aalborg University, Denmark, from January to February 2018. He is currently a Research Professor with the Department of Electrical Engineering, Yeungnam University. His research interests include ac–dc converters, dc–ac inverters, and electric vehicle battery chargers.

Dong-Choon Lee (Senior Member, IEEE) received the B.S., M.S., and Ph.D. degrees in electrical engineering from Seoul National University, Seoul, South Korea, in 1985, 1987, and 1993, respectively.

He was a Research Engineer with Daewoo Heavy Industry, Seoul, South Korea, from 1987 to 1988. He has been a Faculty Member with the Department of Electrical Engineering, Yeungnam University, Gyeongsan, South Korea, since 1994. He was a Visiting Scholar with the Power Quality Laboratory, Texas A&M University, College Station, TX, USA, in 1998; the Electrical Drive Center, University of Nottingham, Nottingham, U.K., in 2001; the Wisconsin Electric Machines and Power Electronics Consortium, University of Wisconsin, Madison, WI, USA, in 2004; and the FREEDM Systems Center, North Carolina State University, Raleigh, NC, USA, from September 2011 to August 2012. His research interests include power converter design and control, renewable energy and its grid connection, ac machine drives, and dc power system.

Dr. Lee served as the Editor-in-Chief for the *Journal of Power Electronics* of the Korean Institute of Power Electronics (KIPE), from January 2015 to December 2017. He served as the President of KIPE in 2019.

Frede Blaabjerg (Fellow, IEEE) received the honoris causa degree from the University Politehnica Timisoara, Timisoara, Romania, and Tallinn Technical University, Tallinn, Estonia, and the Ph.D. degree in electrical engineering from Aalborg University, Aalborg, Denmark, in 1995.

He was with the ABB-Scandia, Randers, Denmark, from 1987 to 1988. He became an Assistant Professor in 1992, an Associate Professor in 1996, and a Full Professor of power electronics and drives in 1998. In 2017, he became a Villum Investigator. He has authored/coauthored more than 600 journal papers in the fields of power electronics and its applications. He has coauthored four monographs and is an editor of ten books in power electronics and its applications. His research interests include power electronics and its applications such as in wind turbines, PV systems, reliability, harmonics, and adjustable speed drives.

Prof. Blaabjerg was the recipient of the 32 IEEE Prize Paper Awards, the IEEE PELS Distinguished Service Award in 2009, the EPE-PEMC Council Award in 2010, the IEEE William E. Newell Power Electronics Award 2014, the Villum Kann Rasmussen Research Award 2014, the Global Energy Prize in 2019, and the 2020 IEEE Edison Medal. He was the Editor-in-Chief of the IEEE TRANSACTIONS ON POWER ELECTRONICS from 2006 to 2012. He has been a Distinguished Lecturer for the IEEE POWER ELECTRONICS SOCIETY from 2005 to 2007 and for the IEEE INDUSTRY APPLICATIONS SOCIETY from 2010 to 2011 as well as from 2017 to 2018. In 2019–2020, he serves as the President of the IEEE POWER ELECTRONICS SOCIETY. He is also the Vice-President of the Danish Academy of Technical Sciences. He was nominated in 2014–2019 by Thomson Reuters to be between the 250 most-cited researchers in engineering in the world.